PHILOSOPHICAL TRANSACTIONS A

rsta.royalsocietypublishing.org

Research

Article submitted to journal

Subject Areas:
climatology, applied mathematics, computational mathematics

Keywords:
climate modelling, ENSO, delay differential equations, bifurcation analysis, non-constant delays

Author for correspondence:
Bernd Krauskopf
e-mail: b.krauskopf@auckland.ac.nz

The effect of state dependence in a delay differential equation model for the El Niño Southern Oscillation

Andrew Keane[1], Bernd Krauskopf[1] and Henk A. Dijkstra[2]

[1]Department of Mathematics, The University of Auckland, Private Bag 92019, Auckland 1142, New Zealand
[2]Institute for Marine and Atmospheric Research Utrecht and Center for Complex Systems Studies, Department of Physics, Utrecht University, Utrecht, The Netherlands

Delay differential equations (DDEs) have been used successfully in the past to model climate systems at a conceptual level. An important aspect of these models is the existence of feedback loops that feature a delay time, usually associated with the time required to transport energy through the atmosphere and/or oceans across the globe. So far, such delays are generally assumed to be constant. Recent studies have demonstrated that even simple DDEs with nonconstant delay times, which change depending on the state of the system, can produce surprisingly rich dynamical behaviour. Here, we present arguments for the state dependence of the delay in a DDE model for the El Niño Southern Oscillation phenomenon in the climate system. We then conduct a bifurcation analysis by means of continuation software to investigate the effect of state dependence in the delay on the observed dynamics of the system. More specifically, we show that the underlying delay-induced structure of resonance regions may change considerably in the presence of state dependence.

THE ROYAL SOCIETY PUBLISHING

1. Introduction

Feedback loops are an important component of climate systems (see [1] and references therein), whereby changes or inputs are either amplified or dampened by nonlinear processes. Such feedback loops are crucial ingredients in climate models [2–7] and they are associated with delay times due to transportation times of mass or energy over large distances. These time delays are generally large compared to the characteristic forcing time scales of the system under consideration. As such, time delays tend to play a vital role in the behaviour of the system.

This is certainly true for delayed feedback loops that arise in the equatorial coupled ocean-atmosphere system governing the El Niño Southern Oscillation (ENSO) phenomenon. This system consists of an atmospheric component, known as the Southern Oscillation, and an oceanic component, El Niño. The El Niño events are characterised by large increases in sea surface temperature (SST) in the equatorial Pacific Ocean, and they occur sporadically approximately every 4–7 years. Large drops in eastern-Pacific SST represent the cool phase and are known as La Niña events. It is well known that El Niño events generally tend to occur near Christmas time. The seasonal cycle (with a period of 1 year) represents the characteristic forcing time scale of the ENSO system. Feedbacks due to ocean-atmosphere coupling processes in the eastern and central equatorial Pacific Ocean have delay times of many months due to the time needed for equatorially trapped waves to propagate across the Pacific Ocean.

El Niño and La Niña events have major consequences all over the globe, yet they are notoriously difficult to predict accurately, even with highly sophisticated global climate models [8,9]. Over many decades, conceptual climate models have proven extremely useful in providing fundamental insights into the inner workings of climate systems; for example, see [10–14]. Conceptual ENSO models have played an important role in building a theory of how El Niño events are created and how they eventually die away, although there are many aspects still open to debate and investigation [12].

A prominent paradigm for how El Niño events form and abate is the so-called delayed action oscillator (DAO), first introduced by Suarez and Schopf [15]. According to this paradigm, feedback loops due to the ocean-atmosphere coupling are crucial in shaping ENSO dynamics. A central ingredient of these feedback loops is the depth of the thermocline, which is a thin layer in the ocean separating deeper cold waters from shallower warm surface water. Another ingredient is the equatorial upwelling which is caused by the surface winds (trade winds) through a mass divergence away from the equator caused by the Earth's rotation (Ekman upwelling). Let the variable $h(t)$ denote the deviation from a long-term thermocline mean in the eastern equatorial Pacific. A positive value of h leads to less water from below the thermocline reaching the sea surface through upwelling, thus an increased SST in the eastern Pacific. This provides a positive feedback because the warm SST anomaly slows down the easterly trade winds since warm air rises and has to be compensated, leading to westerly wind anomalies, deepening the thermocline. The positive anomalous thermocline depth signal at the equator is carried to the eastern boundary of the ocean via so-called Kelvin waves. Off the equator, the negative anomalous thermocline depth signal is carried to the western boundary of the ocean via so-called Rossby waves. These waves are reflected as Kelvin waves, which carry the shallow thermocline perturbation back to the eastern boundary of the ocean, completing a negative feedback loop.

There exist a number of models based on the DAO paradigm; for example, see [15–18]. The DDE model introduced by Ghil, Zaliapin and Thompson [19] is one of the simplest in that it focusses on the interaction between the negative delayed feedback and additive seasonal forcing. Neglecting the above-mentioned positive feedback is not necessarily justified in [19], rather it is done in order to demonstrate that the other two terms are sufficient to produce very rich dynamical behaviour relevant to ENSO. The effect of re-introducing the positive delay feedback to this model is studied in detail in [20]. The model from [19] takes the form

$$\frac{d}{dt}h(t) = -b\tanh[\kappa h(t-\tau_n)] + c\cos(2\pi t). \tag{1.1}$$

The parameters b and c are amplification factors of the negative feedback and seasonal forcing terms, respectively. The ocean-atmosphere coupling is of a particularly simple form, $\tanh(\cdot)$, with the coupling strength κ as the only parameter; see the study [21] for a justification and for a variation with different asymptotes. Originally, a different coupling function, a cubic, was chosen in [15,16,22]. The additive form of the forcing is chosen for simplicity and is open to debate; for example, parametric seasonal forcing was considered in a simple DDE ENSO model in [18]. Here the effect of the seasonal forcing is assumed to be instantaneous, as has been the case in all previous literature. The delay time τ_n arises from the Rossby and Kelvin waves closing the negative feedback loop, and it is assumed to be constant in all previous work. In some literature, model (1.1) is also referred to as the GZT model.

Modelling with DDEs is built on the idea that only the delayed effect of a chain of complex processes needs be modelled, and not the processes themselves — resulting in a convenient model reduction. The resulting DDE model is capable of complicated behaviour, yet is still amenable to sophisticated mathematical analysis. In the case of model (1.1), only the delayed effect of the negative feedback is included, while a full description (for example, by partial differential equations) would involve many more variables and parameters relating to zonal wind anomaly, surface pressure anomaly, thermal damping coefficients, etc. The GZT model is deceivingly simple in that it features only delayed feedback and periodic forcing. Yet, it was shown in [19,23] to be capable of dynamics that could replicate certain ENSO features, such as variability on appropriate time scales and phase locking with the seasons. These are features that have been observed earlier in more complex ENSO models [24–26]. The balance between the complicated dynamics produced by DDE models and their (relative) simplicity, allowing them to still be mathematically tractable, explains their success in areas as diverse as, for example, laser dynamics [27], neural networks [28], traffic flow [29], cell population dynamics [30] and epidemics [31].

DDEs are infinite-dimensional dynamical systems and their analysis generally poses analytical and numerical challenges. Nonetheless, the theory of DDEs with a finite number of constant delays is well developed [32,33]. In fact, the bifurcation theory of constant-delay DDEs is analogue to that of ordinary differential equations: their solutions depend smoothly on parameters, and initial conditions and their linearisations around equilibria and periodic solutions have at most finitely many unstable eigendirections. Furthermore, advanced numerical tools for their simulation and bifurcation analysis are available and have been successfully applied to analyse models arising in various applications; for example, see [34] and references therein.

In [20,35] we conducted a bifurcation analysis of the GZT model (1.1) in order to understand how it is able to produce such rich dynamics. This was done by means of the MATLAB based continuation software DDE-Biftool [36,37], which allows the user to track (or continue) steady-state and periodic solutions of DDEs while varying a chosen model parameter. It can calculate the stability of such solutions, allowing one to detect bifurcations. It is then possible to continue detected bifurcations of steady-state and periodic solutions in two-parameter planes. The bifurcation analysis in [35] revealed that in the (c, τ_n)-plane the dynamics of the GZT model can be divided roughly into three parameter regions where the dynamics is: (i) periodic due to the negative delayed feedback alone, (ii) periodic and dominated by the seasonal forcing, and (iii) an interplay of both mechanisms. In the latter case, one finds dynamics on an invariant torus, which may be locked (periodic) or unlocked (quasiperiodic). The periodic solutions on the torus are organised in the parameter plane into p:q resonance tongues; where they wind around the torus to form p:q torus knots. It was shown in [35] that there exist small regions in the (c, τ_n)-plane where multiple resonance tongues overlap. In these regions period-doubling cascades and chaotic solutions exist.

Of course, the use of a constant value for any delay in a DDE model, such as the GZT model, is a modelling assumption. A recent review on the use of DDEs in conceptual climate models [38] confirms that the delays in DDE climate models have generally been assumed to be constant. While this assumption is well justified in certain applications, such as machining [39] and laser

dynamics [40], delays in many applications are definitely not constant. Often the delay times will depend on the state of the system itself, which leads to DDE models with state-dependent delays. The theory of and numerical methods for state-dependent DDEs is more difficult and still under development [37,41–43].

Recently, Calleja *et al.* [44] studied the dynamics of a simple scalar DDE where two delay times depend linearly on the state of the system. The associated constant-delay DDE is linear and capable of only trivial dynamics. However, with state dependence of the delays the system generates surprisingly complicated dynamics, as was demonstrated by a combination of numerical continuation and normal form calculations. In light of this study, we must ask whether, after nearly 40 years of DDE climate models, is it still a safe modelling assumption to take their delay times as constant?

This paper contributes by studying the effect of state dependence on the dynamics of model (1.1). We introduce these effects in a heuristic fashion in the hope that our results will provide motivation for a more thorough and quantitative derivation of state dependence in ENSO. This would involve either the analysis of more complex model equations or data from such models or observations. More generally, this paper can be considered as a first step in addressing two fundamental questions:

(1) When do state-dependent delay arise in climate variability phenomena and what mathematical forms do they take?
(2) Does the state dependence in the delay have a significant effect on the behaviour of the solutions of delay-equation models of these phenomena?

One reason to choose model (1.1) as a test-case example is that its bifurcation analysis in the (c, τ_n)-plane, presented in [35], provides a good starting point for observing the influence of state dependence on model behaviour. In spite of its simplicity among DAO models, the constant-delay GZT model already features complicated resonance phenomena. Moreover, model (1.1) can be viewed as prototypical in that it describes the interplay between delayed negative feedback and periodic forcing. Therefore, the results presented here may provide insight into whether or not state dependence of delays is important also in the context of other climate models, as well as applications from other fields. For example, DDE models of similar form can be found in human motion control [45], network dynamics [46] and laser dynamics [47]. Recently, the importance of incorporating state dependence in modelling has been recognised in turning processes [48], physiology [49] and lasers with frequency-dependent feedback [50,51].

We begin with considering in some detail how non-constant delay times in the negative feedback loop arise from the physics of the ocean-atmosphere coupling. Here we focus on how the surface of the ocean couples with the thermocline below. This leads to two different delay terms with state dependence. The first, denoted τ_c, is due to the coupling process in the central equatorial Pacific Ocean, and it depends linearly on the current thermocline depth $h(t)$. The second, denoted τ_e, is due to coupling processes in the East and depends linearly on the state h in the past. Overall, we obtain a state-dependent version of model (1.1) with two extra parameters that allow us to 'switch on' these two types of state dependence; as part of our modelling we also discuss realistic ranges for the respective state dependence. We present bifurcation sets in the $(c, \bar{\tau}_n)$-plane that demonstrate the effect of the two types of state dependence, first individually and then in combination; here $\bar{\tau}_n$ is the constant part of the now state-dependent delay. As the starting point for our study, we first briefly review the bifurcation set in the $(c, \bar{\tau}_n)$-plane for the constant delay case from [35]. It turns out that, over the range we consider, the state-dependent term τ_e alone has a negligible effect on the bifurcation set. The term τ_c, on the other hand, has a significant impact on the resonance regions in the $(c, \bar{\tau}_n)$-plane: we find reconnecting torus bifurcation curves, considerable increases of certain resonance regions and much more overlapping between resonance regions and associated period-doubling cascades. Interestingly, in the presence of state dependence in τ_c, the state-dependent term τ_e does have a considerable influence on the bifurcation set, increasing the observed complexity even further. This includes

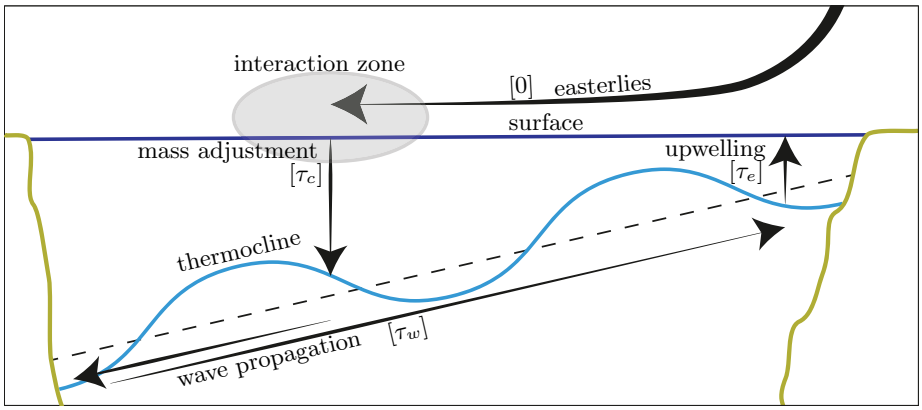

Figure 1. Schematic diagram of ocean-atmosphere interaction in the central and eastern equatorial Pacific Ocean following perturbations to the thermocline depth in the eastern equatorial Pacific. The dashed line represents the mean thermocline depth.

the breaking of a reflection symmetry, which in the past was only achieved by introducing an asymmetric coupling function [18,20,21]. Overall, we find for realistic levels of state dependence a bifurcation set that is much more complex than its constant-delay counterpart. In particular, a computation of Lyapunov exponents shows that there are considerably larger parameter regions with chaotic behaviour associated with overlapping resonance regions. Since this type of complicated and irregular behaviour has been identified as showing important characteristics of ENSO, we argue that state dependence in model (1.1) emerges as an important ingredient for a more realistic description of its underlying feedback mechanisms.

The paper is organised as follows. In Section 2 we discuss how the delay time in model (1.1) can be modified to include two state-dependence terms that arise from surface-thermocline interaction. The resulting dynamics is studied in Section 3, where we review the constant-delay case in Section 3(a), consider each state-dependence term individually in Section 3(b), and then in combination in Section 3(c). Finally, in Section 4 we make some concluding remarks and point out future research directions.

2. State dependence of the delay in model (1.1)

We now motivate the inclusion of state-dependent terms into the delay time of model (1.1). There are various potential sources of state dependence in the ENSO system. The type of state dependence we present here arises from the interaction times between the thermocline and the sea surface, which are not described by and go beyond the original DAO mechanism.

The idea that both wave dynamics and thermocline-SST interactions are important for accurately describing ENSO behaviour is supported by [52–55]. More specifically, the state-dependent DDE model (1.1) presented in this section, with the state-dependent delay given by (2.6), is related to previous conceptual-level models for ENSO with underlying physics that can be traced back to the Zebiak-Cane model [56]. As summarized by Dijkstra [4, Section 7.5.4], applying slightly different assumptions to equations derived from the intermediate-complexity Zebiak-Cane model will lead to the DAO, as well as the coupled wave oscillator [22] and the recharge oscillator [57,58]. Each of these ENSO paradigms describes the negative feedback and the propagation of oceanic waves, albeit in different mathematical forms. The coupled wave oscillator model [22] assumes that the effect of the thermocline depth on the SST in the East is instantaneous. The DAO and recharge oscillator do not make this assumption. However, neither attempt to resolve thermocline-SST interactions to include the effect of an evolving thermocline.

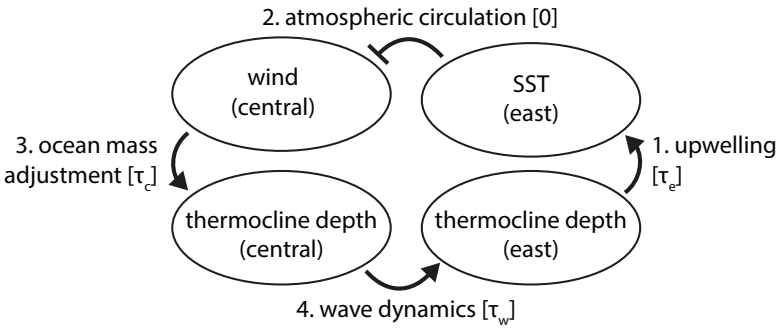

Figure 2. Flow diagram of the negative delayed feedback due to ocean-atmosphere coupling; all quantities involved represent deviations.

As we will see in the following section, this is an effect that can have important consequences for the behaviour of the system.

(a) Components of the negative feedback

Figure 1 is a schematic diagram of ocean-atmosphere coupling processes in the central and eastern equatorial Pacific Ocean that are involved in the negative feedback loop of ENSO. The horizontal direction represents longitude and the vertical direction represents depth. The dark blue curve represents the ocean surface and the light blue curve the thermocline layer, the yellow curves indicate the basin boundaries of the Pacific Ocean, and the grey ellipse represents a coupling interaction zone. In its mean state the thermocline depth, which is indicated by the dashed line, is shallower in the East (about 50 metres) compared to the depth in the central equatorial Pacific Ocean (about 150 metres). The black arrows represent the four components of the negative feedback: upwelling in the East, easterly winds, ocean adjustment in the central Pacific, and wave propagation. Each component is associated with a delay time that appears in square brackets in Figure 1.

The overall negative feedback loop is represented in Figure 2 as a flow diagram. Its first component consists of a positive perturbation in the thermocline depth in the eastern equatorial Pacific that increases the SST in the eastern equatorial Pacific. This happens via an upwelling process with associated delay time τ_e. Next, the increase in SST slows down the easterly trade winds, creating a westerly wind anomaly over the central equatorial Pacific. This is a fast process and it is assumed here not to be subject to a delay (as is the case in all DAO models). The wind anomaly induces an ocean mass adjustment that decreases the thermocline depth in the central equatorial Pacific. This occurs in a reasonably localised interaction zone, and in mathematical derivations of DAO models [22,58] this zone is simplified to a point. The associated surface-thermocline interaction comes with a delay time τ_c. Rossby waves then carry the signal to the western basin boundary and are reflected as Kelvin waves, which carry the signal back to the East with an associated delay time τ_w. The total delay time associated with the negative feedback loop is therefore

$$\tau_n = \tau_e + \tau_c + \tau_w. \tag{2.1}$$

In past studies of DAO models, the delay time τ_n associated with the negative feedback has been assumed to consist only of τ_w, which is taken to be constant. We now take into account also the processes of upwelling and ocean adjustment and the associated delay times τ_e and τ_c, as sketched in Figures 1 and 2. Importantly, while they are on average smaller than τ_w, we argue now that τ_e and τ_c are relevant and, in particular, that they depend on the state. The underlying principle is that the distance the signal must travel to or from the surface depends on the depth of the thermocline as represented by its deviation h from it long-term average.

(b) State dependence due to upwelling

There is a delay, indicated by τ_e in Figure 2, between the thermocline anomaly at depth and the SST anomaly at the surface; this is due to upwelling of colder water. We model this effect by

$$\tau_e = \bar{\tau}_e + \eta_e h(t - \tau_n), \tag{2.2}$$

where $\bar{\tau}_e$ is the constant delay time it takes the signal to travel from the mean thermocline depth to the surface and η_e is the inverse of the upwelling speed. The delay time τ_e deviates from its mean value by $h(t - \tau_n)$ because the thermocline depth signal that ultimately returns to the eastern equatorial Pacific at time t began its journey at the thermocline at time $t - \tau_n$. Notice that this means that the state-dependent delay in (2.2) is, hence, defined only implicitly. To avoid this issue we consider the first-order approximation of replacing the state-dependent τ_n with its constant part $\bar{\tau}_n = \bar{\tau}_e + \bar{\tau}_c + \tau_w$, where $\bar{\tau}_c$ is the constant delay time of the ocean adjustment at the central Pacific associated with the mean thermocline depth (see the next section). This yields the upwelling delay in the delayed form

$$\tau_e = \bar{\tau}_e + \eta_e h(t - \bar{\tau}_n). \tag{2.3}$$

(c) State dependence due to ocean adjustment

We now address the delay between the SST and thermocline depth anomalies in the central equatorial Pacific Ocean, represented by the third component of the feedback loop in Figure 2. This can be attributed to a basin adjustment involving a collection of waves, which can be viewed as an adjustment to Sverdrup balance at off-equatorial latitudes. This adjustment is a crucial element in the so-called recharge-oscillator view of El Niño [57,58]. Due to the westerly wind-stress anomaly, which is arising through a positive SST anomaly, mass is diverging out of the equatorial zone because of this Sverdrup adjustment. Note that, although the associated arrow in Figure 1 points downward to show the direction of the feedback loop, there is actually mass adjustment both in and out of the equatorial zone. Only after an adjustment time τ_c will this have an effect on the thermocline depth. Because the mass transport is dependent on the thermocline depth, so is τ_c. We model this effect here by

$$\tau_c = \bar{\tau}_c + \eta_c h_c(t - \tau_w), \tag{2.4}$$

where $h_c(t - \tau_w)$ is the thermocline anomaly in the central Pacific Ocean and $\bar{\tau}_c$ is the constant component associated with the mean thermocline depth. By neglecting damping effects on the oceanic waves that carry the feedback signal back to the eastern Pacific Ocean, we can use the approximation $h_c(t) \approx h(t + \tau_w)$ in (2.4). This results in the ocean adjustment delay having the non-delayed form

$$\tau_c = \bar{\tau}_c + \eta_c h(t), \tag{2.5}$$

(d) Total delay time

From (2.1) the total state-dependent delay then takes the form

$$\tau_n(h) = \bar{\tau}_n + \eta_e h(t - \bar{\tau}_n) + \eta_c h(t). \tag{2.6}$$

The resulting state-dependent ENSO DDE model we consider in what follows is model (1.1) with the delay as given by (2.6). Clearly, this overall model reduces to the constant-delay GZT model for $\eta_e = \eta_c = 0$. However, for $\eta_e \neq 0$ or $\eta_c \neq 0$ state dependence is present and must be taken into consideration. In particular, we remark that, as with any state-dependent DDE, the delay τ_n must remain positive for the evolution to be well defined. We will see later that in some parameter regions τ_n becomes negative along solutions; when this is identified during numerical integration (we employ an improved Euler method with fixed time steps) the computation is stopped.

(e) Suitable parameter ranges

Based on the correlation analysis of observational SST and thermocline depth data by Zelle *et al.* [59], we estimate the constant delay times $\bar{\tau}_e$ and $\bar{\tau}_c$ to be 2 weeks and 4 months, respectively.

The maximum deviations in the thermocline depth in the eastern equatorial Pacific Ocean correspond to about 50 metres [60], which is also the mean thermocline depth, suggesting that $\max[\eta_e h(t-\tau_n)] \approx 2$ weeks. Since in the GZT model, the maximum values of $h(t)$ are of order 1 and time is in years, we obtain the nominal value of $\eta_e \approx 2/52 \approx 0.04$. Similarly, the maximum deviations in thermocline depth in the central equatorial Pacific Ocean corresponds to about one third of its mean depth, suggesting that $\max[\eta_c h(t)] \approx 4/3$ months. Therefore, we obtain the nominal value $\eta_c \approx (4/3)/12 \approx 0.11$.

We use these nominal values for η_e and η_c in the bifurcation analysis in the next section. In light of various approximations and uncertainties, and to present a more comprehensive picture of the possible dynamics, we also consider the bifurcation set for twice these values, namely for $\eta_e = 0.08$ and $\eta_c = 0.22$.

Finally, based on oceanic wave speeds calculated using TOPEX/POSEIDON satellite data in [61,62], realistic values of τ_w lie between 5.2 and 7.2 months, that is, in the range $[0.43, 0.6]$ when scaled to years. This places the estimated range for $\bar{\tau}_n$ at $[0.80, 0.97]$. Nonetheless, in the following section we choose to consider the parameter range $[0, 2]$ for two reasons: (i) to allow a comparison with previous literature [19,20,23,35]; and (ii) to understand the global origins of observed complex dynamics.

3. Bifurcation analysis

To demonstrate how the two types of state dependence affect the behaviour of model (1.1), we now present bifurcation sets in the $(c, \bar{\tau}_n)$-plane of (1.1) with (2.6) for different values of η_e and η_c. These consist of curves of torus bifurcations, saddle-node of limit cycle bifurcations and period-doubling bifurcations, all computed with the continuation package DDE-BIFTOOL [36,37]. These curves are overlaid onto so-called maximum maps, where the maxima of long time series (after transients have died down) are computed and represented in colour for fixed $\bar{\tau}_n$ and increasing c (where the previous solution serves as initial history); we typically compute a trajectory of 1000 years and disregard the first 500 years, where the integration step is 10^{-4} years. Maximum maps allow for a ready comparison with previous studies of the GZT model [19,23,35], and we fix throughout $b = 1$ and $\kappa = 11$ as in these previous works. Moreover, the bifurcation set in the $(c, \bar{\tau}_n)$-plane provides a clear overview of how the dynamics is organised more globally.

In Section 3(a) we give a brief review of the findings in [35] for the constant-delay case $\eta_e = \eta_c = 0$. We then "switch on" and increase the state dependence by presenting the bifurcation set for nonzero η_e and η_c. We first consider their effects individually in Section 3(b), and then in combination in Section 3(c). Finally, we briefly discuss in Section 3(d) how the results could be interpreted in the context of the ENSO phenomenon.

(a) The constant-delay case

Figure 3 shows the bifurcation set in the $(c, \bar{\tau}_n)$-plane for the constant-delay case $\eta_e = \eta_c = 0$, overlaid onto the maximum map. The maximum map provides a convenient indication of the respective behaviour. Notice that sudden changes in colour, that is, in the maximum value of h on an attractor, align well with shown bifurcations. Periodic solutions born along the line $c = 0$ are stable and have non-zero amplitude for $\bar{\tau}_n > \pi/(2\kappa)$ [63–65]; these are dominated by the effect of negative feedback and have a period of $4\bar{\tau}_n$. On the other hand, for sufficiently large values of c there are stable periodic solutions that are dominated by the seasonal forcing. These solutions appear to be close to sinusoidal and have a period of one; for decreasing c, they lose their stability at the torus bifurcation curve. Between the line $c = 0$ and the torus bifurcation curve solutions are characterised by an interplay between negative feedback and periodic forcing,

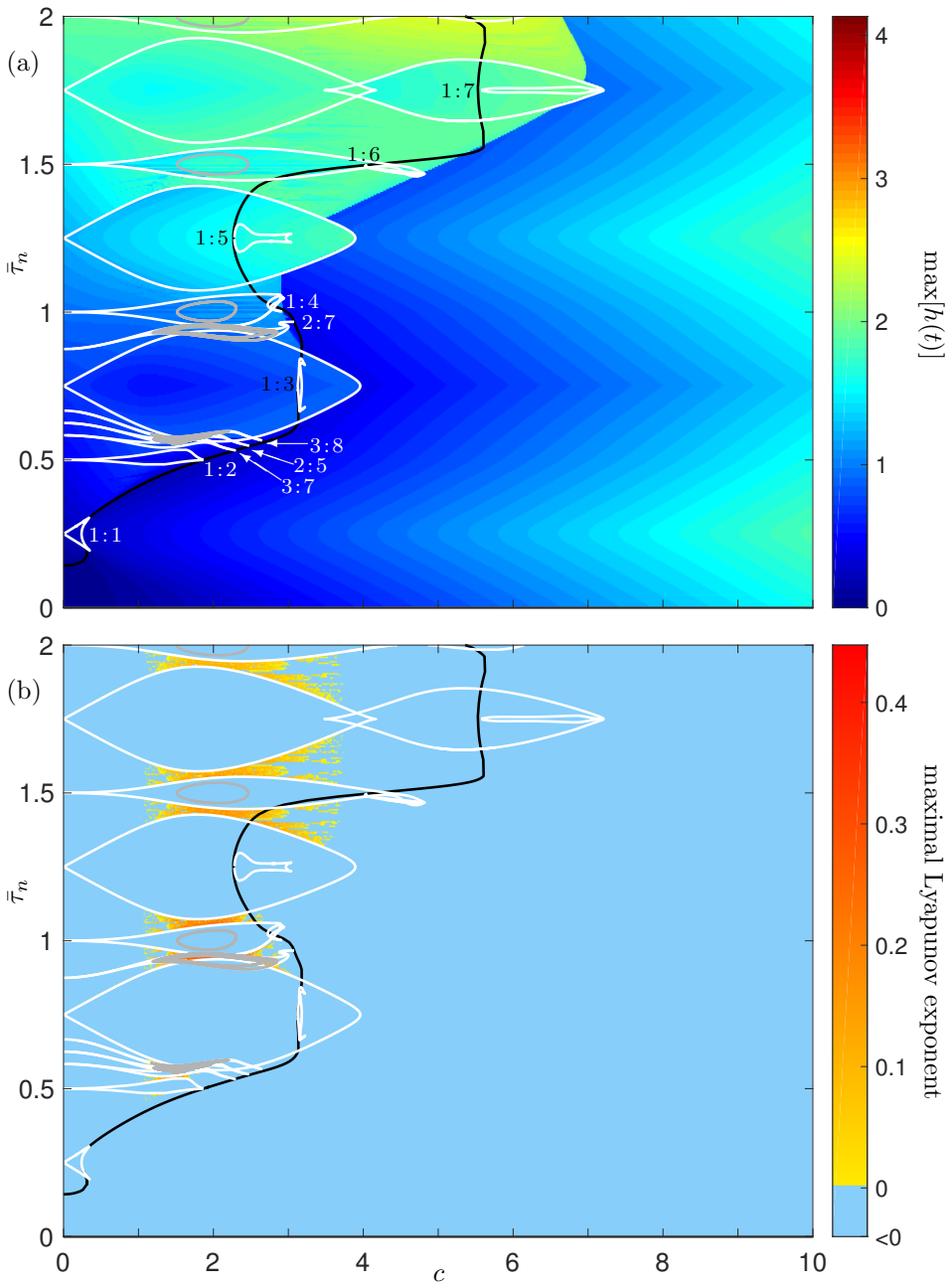

Figure 3. Bifurcation set with maximum map (a) and positive maximal Lyapunov exponent (b) in the $(c, \bar{\tau}_n)$-plane of Eq. (1.1) with (2.6) for the constant-delay case $\eta_e = \eta_c = 0$ in Eq. (2.6). Shown is a black curve of torus bifurcations, white curves of saddle-node bifurcations of periodic orbits that bound p:q resonance tongues, and grey curves of period-doubling bifurcations. The simulation scans here and throughout the paper are performed for fixed $\bar{\tau}_n$ and increasing c.

resulting in dynamics on invariant tori. As was mentioned in Section 1, the dynamics on the torus may be locked (periodic) or unlocked (quasiperiodic). The locked solutions are organised into p:q resonance tongues, where p/q is the *winding number* of the periodic solutions, of which there is generally a stable and an unstable one on the torus. Theory predicts an infinite number of

resonance tongues, one for every rational winding number [66], and Figure 3 shows a set of the largest resonance tongues. As could be expected from the mathematical form of model (1.1), the dependence of the solutions on the parameters appears to be highly nonlinear.

Inside some of the shown resonance tongues, period-doublings are found. This is a common feature when resonance tongues overlap sufficiently; for a detailed study of accumulating resonance tongues and associated complex behaviour see [67]. The resulting chaotic behaviour is of interest in the context of ENSO, since such behaviour shows a mixture of irregularity with locking to the seasons, which is seen as characteristic for El Niño and La Niña events in the real world. Note that period-doubling cascades and associated chaotic dynamics are found only in small regions of the parameter plane; see panel (b) showing where the respective maximal Lyapunov exponent is positive, as calculated by following the algorithm for DDEs in [68]. Regions of positive maximal Lyapunov exponents are also observed for parameters where we show no curves of period-doublings. This is simply because there exist higher-order resonance tongues in between those we have shown and they are expected to overlap. Furthermore, as demonstrated for a related DDE model in [20], chaotic regions are often bound not only by period-doubling cascades, but also feature intermittent transitions that are characterised by the sudden appearance of chaos at a saddle-node bifurcation [69]. A more comprehensive discussion of the bifurcation set in Figure 3 and associated other types of dynamics, including multistability, changing criticality of the torus bifurcation and folding tori, can be found in [35,70].

(b) Individual effects of the two types of state dependence

Considering only the state dependence of the upwelling delay τ_e, we find the anticlimactic result that it does not appear to have an influence on the observed dynamics. More specifically, for $\eta_e = 0.04$ and $\eta_e = 0.08$ and with $\eta_c = 0$ in (2.6), bifurcation set and maximum map in the $(c, \bar{\tau}_n)$-plane do not show any observable change on the scale presented in Figure 3.

State dependence of the ocean mass adjustment alone, on the other hand, does have a dramatic effect. Figure 4 shows the bifurcation sets and maximum maps for fixed $\eta_e = 0$ and for $\eta_c = 0.11$ in panel (a) and for $\eta_c = 0.22$ in panel (b). Already for $\eta_c = 0.11$ the difference with the case of $\eta_c = 0$ in Figure 3 is striking: resonance tongues have become wider and overlap more, with larger regions where one finds period-doublings. The torus bifurcation curve now extends to $c = 10$ near the top of Figure 4(a), and there is a noticeable change in the size of the observed maxima. Moreover, there is a region with complex dynamics and additional saddle-node and torus bifurcation curves that entered the frame at large value of c above $\bar{\tau}_n = 1$. These are caused by the state dependence — large c values mean large amplitude, which leads to larger fluctuations of the delay time τ_n. In fact, due to the scaling relationship between c and η_c as a result of Equation (2.6), it is clear that these curves will diverge off to $c \to \infty$ as $\eta_c \to 0$; similarly, they move closer to the other bifurcation curves as η_c increases. The existence of nontrivial dynamics for large values of c is in stark contrast to the dynamics in the constant-delay case, where solutions for sufficiently large c are trivially dominated by the periodic forcing.

Figure 4(b), now for $\eta_c = 0.22$, shows a considerably more complicated bifurcation set compared to panel (a). The bifurcation curves that emerge from the right-hand side of panel (a) have shifted towards lower values of c in panel (b), such that they now interact with the pre-existing structure of resonance tongues. This gives rise to many more and overlapping resonance tongues that extend all the way to large values of c near $\bar{\tau}_n = 1$. In this region we find many and overlapping curves of subsequent period-doublings, which we refer to here as a *period-doubling cluster*. In this part of the $(c, \bar{\tau}_n)$-plane there are not only period-doubling cascades inside resonance tongues, but also a period-doubling cascades of the $0{:}1$ periodic solutions, that is, those dominated by the seasonal forcing. Also near $\bar{\tau}_n = 1$, as well as near $\bar{\tau}_n = 2$, we observe curves of saddle-node bifurcations of $0{:}1$ periodic solutions, which meet at a cusp bifurcation at $(c, \bar{\tau}_n) \approx (5.3, 1)$ (which is not so easy to see due to the many surrounding bifurcation curves) and at $(c, \bar{\tau}_n) \approx (5.3, 2)$, respectively.

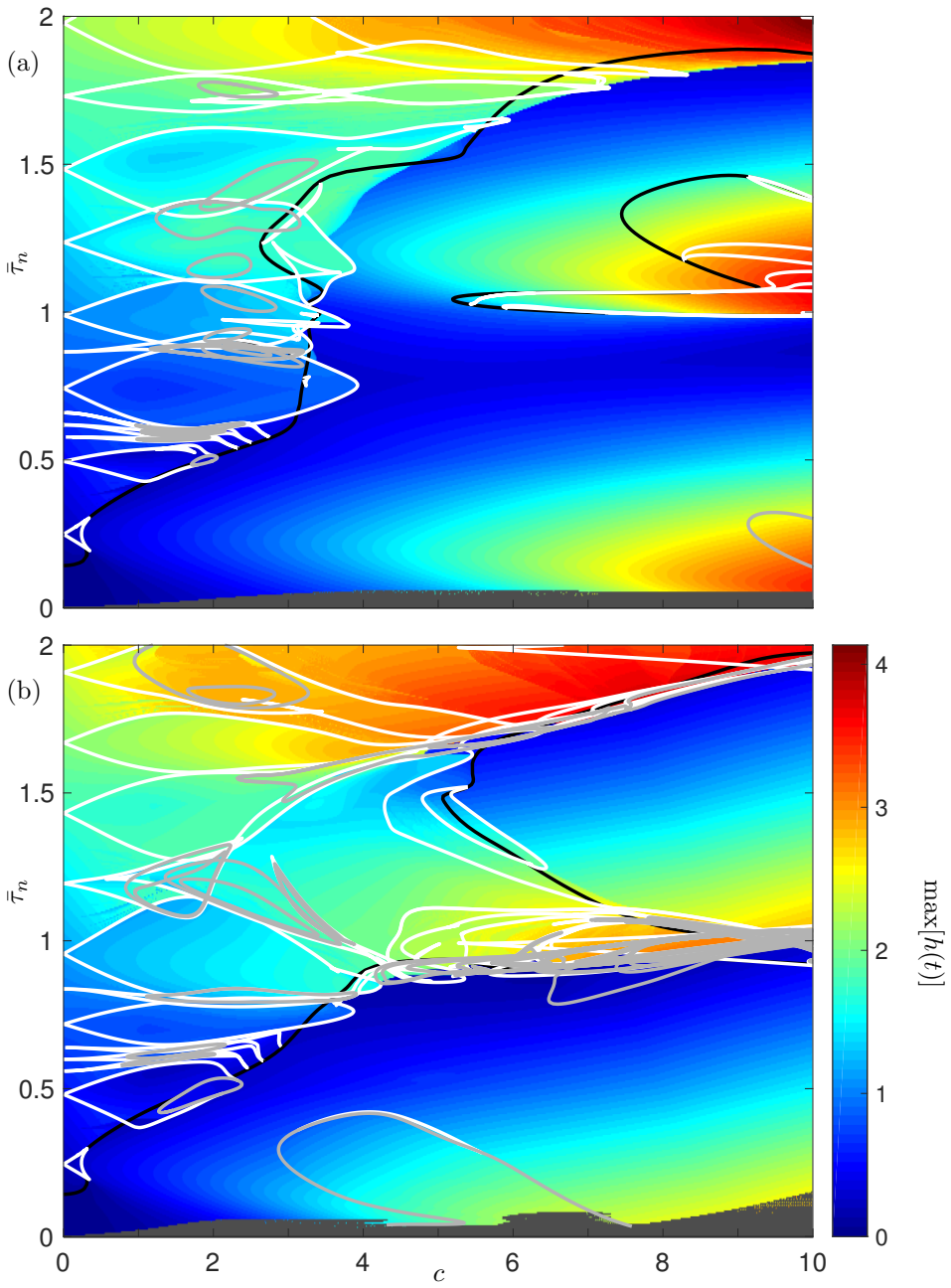

Figure 4. Bifurcation set and maximum map in the $(c, \bar{\tau}_n)$-plane of Eq. (1.1) with (2.6) for $\eta_c = 0.11$ (a) and $\eta_c = 0.22$ (b) and for fixed $\eta_e = 0$. Shown are black curves of torus bifurcations, white curves of saddle-node bifurcations of periodic orbits and grey curves of period-doubling bifurcations.

Although the resonance tongues are not individually labelled, a careful comparison between Figures 3 and 4 reveals that, with increasing state dependence, the roots of resonance tongues along the line $c = 0$ have moved to lower values of $\bar{\tau}_n$. Beyond our numerical approach and the scope of our analysis, the resonance tongues can be studied in the limit of small c. For example, the positions and boundaries of the resonance tongues could be estimated by means of a response or sensitivity function approach [71,72].

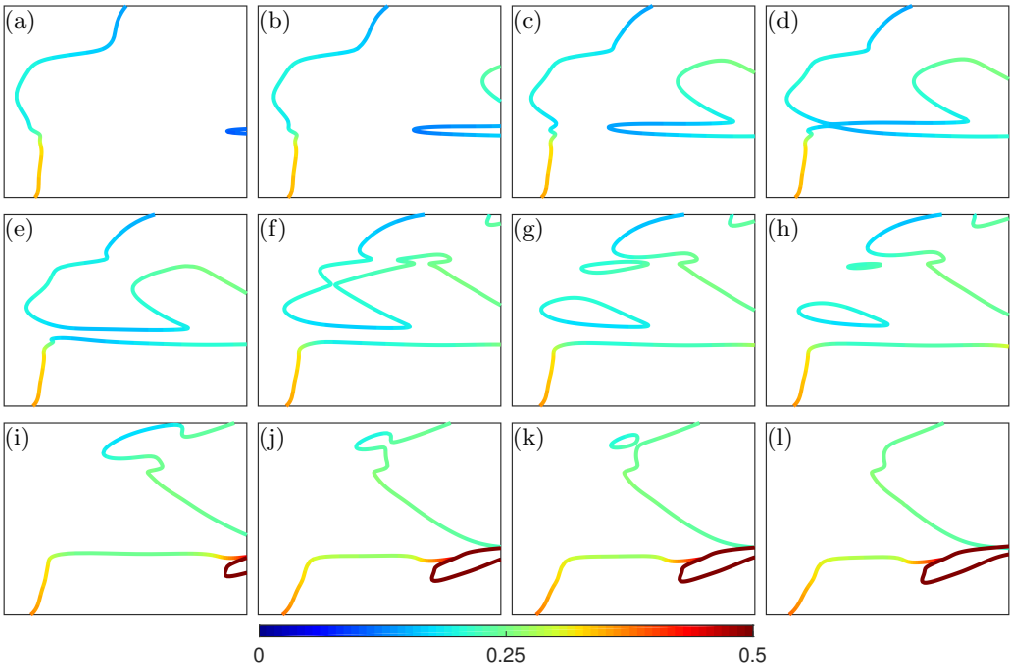

Figure 5. Curves of torus bifurcations in the $(c, \bar{\tau}_n)$-plane in the region $[2, 10] \times [0.6, 1.8]$, where colour indicates the winding number. Here $\eta_e = 0$ and η_c takes the values (a) 0.080, (b) 0.095, (c) 0.110, (d) 0.115, (e) 0.120, (f) 0.130, (g) 0.135, (h) 0.140, (i) 0.155, (j) 0.185, (k) 0.190 and (l) 0.200.

We remark that in a parameter region near $\bar{\tau}_n = 0$ in Figure 4(a) and (b) the delay becomes negative during simulations; this is indicated by grey shading. To resume calculations for the next increment in c, we start the integration from a constant initial history of $h(t) \equiv 10^{-3}$. Similarly, the continuation of the lower period-doubling curve in panel (b) stops when the state-dependent component of the delay becomes so large that the delay becomes negative. The intricate boundary of the grey region of the $(c, \bar{\tau}_n)$-plane already indicates that it depends very sensitively on the initial history whether the delay becomes negative along a trajectory.

The overall resonance structure of the bifurcation sets in Figures 3 and 4 is in some sense organised by the curves of torus bifurcations. In order to provide insight on how the bifurcation set changes qualitatively with η_c for fixed $\eta_e = 0$, Figure 5 presents with twelve panels how the curves of torus bifurcations evolve in the $(c, \bar{\tau}_n)$-plane when η_c is increased gradually from zero. Here the colour scheme indicates the winding number α along the curve, which is given by the complex conjugate pair of Floquet multipliers $e^{\pm 2\pi i\alpha}$ that lie on the unit circle at the moment of torus bifurcation (also known as a Neimark-Sacker bifurcation). As η_c is increased, new curves of torus bifurcations enter the frame from the right [panels (a)–(c)]. They then interact with the torus bifurcation curve that exists already for $\eta_c = 0$ in several codimension-one singularities (of the surface of torus bifurcations in $(c, \bar{\tau}_n, \eta_c)$-space); see, for example, [73] more information on singularity theory. The first such interaction is a saddle-transition at $\eta_c \approx 0.115$, where two curves meet at a single point and then reconnect differently [panels (d)–(e)]. As a result, both curves of torus bifurcations extend to large c near $\bar{\tau}_n = 1$. Two further saddle-transitions just past $\eta_c \approx 0.130$ create two isolas, that is, closed curves of torus bifurcations [panels (f)–(h)]. Note that all these transitions through singularities of the surface are consistent with the colouring by winding number. Subsequently, these isolas shrink down to points and disappear in what we refer to as minimax transitions. Increasing η_c further, we find that a curve of period-doubling bifurcations (dark red) enters the frame, to which the lower branch of torus bifurcations connects at a 1:2 resonance point [panels (i)–(l)].

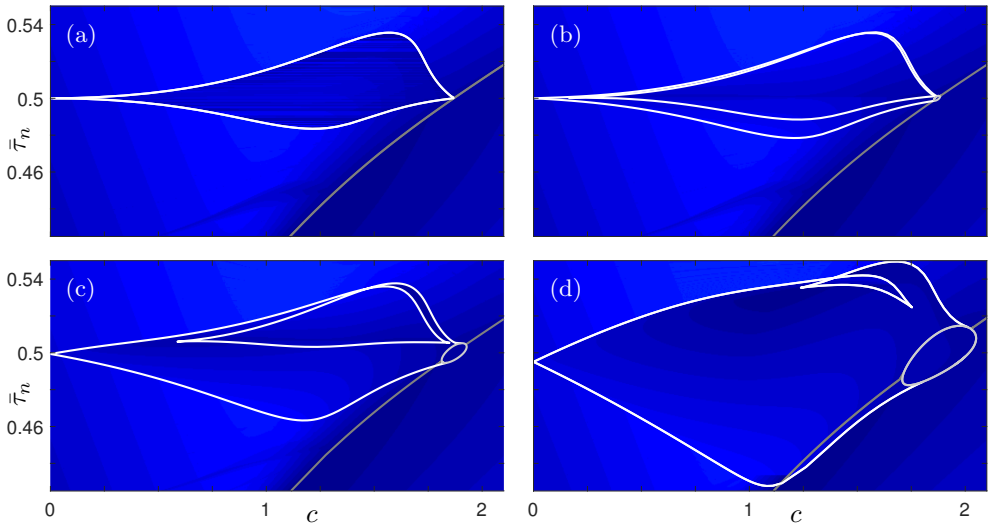

Figure 6. Maximum maps and the $1{:}2$ resonance tongue for $\eta_c = 0$ (a), $\eta_c = 0.01$ (b), $\eta_c = 0.04$ (c) and $\eta_c = 0.11$ (d) and for fixed $\eta_e = 0$. Shown are the white bounding curves of saddle-node bifurcations of periodic orbits, dark grey curves of torus bifurcations and light grey curves of period-doubling bifurcations. For the background colour scheme see Figure 4.

Overall, Figure 5 gives a good indication of how the bifurcation set becomes more complex with increasing η_c. Indeed, the torus bifurcation curves shown come with infinitely many resonance tongues, leading to the overall complexity that was shown in Figure 4. Focusing on only the torus bifurcation curves avoids the considerable computational cost associated with computing many more bifurcation curves and maximum maps. We remark that computing all of the bifurcation curves shown in Figure 4 is not fully automatic but requires an interactive process with DDE-BIFTOOL that takes about 2–4 days per panel; computing the associated maximum map, on the other hand, can be fully parallelised, yet still takes about 4–5 hours on the New Zealand eScience Infrastructure Pan cluster high-performance computing facility.

As was stated above, one of the effects of state dependence is that some of the resonance tongues become larger. To illustrate this effect in more detail, Figure 6 shows how the $1{:}2$ resonance tongue in the $(c, \bar{\tau}_n)$-plane changes for fixed $\eta_e = 0$ and increasing η_c. It demonstrates that the widening of some resonance tongues coincides with a breaking of symmetry. As discussed in [35], the constant-delay GZT DDE model features a $\mathbb{Z}_2$-symmetry: in $p{:}q$ resonance tongues with p or q even, there exist two distinct, symmetrically related periodic locked solutions. The $1{:}2$ resonance tongue in panel (a) is such an example and there are actually two sets of curves of saddle-node bifurcations that lie on top of each other. As η_c is increased, however, they separate more and more, as panels (b)–(d) show. For the $1{:}2$ resonance tongue, this symmetry breaking also results in a closed curve of period-doubling bifurcations being created at the right tip where the resonance tongue connects with the torus bifurcation curve; this curve of period-doubling bifurcations has two $1{:}2$ resonance points where the respective branches of torus bifurcations connect. This phenomenon is actually part of the complicated bifurcation structure near $1{:}2$ resonances predicted by theory; for example, see [66, section 9.5.3]. We remark that this bifurcation structure is also relevant for the period-doubling bifurcations of the seasonal-forcing dominated solutions that emerge near $\bar{\tau}_n = 1$; compare with Figure 5(l) and Figure 4(b).

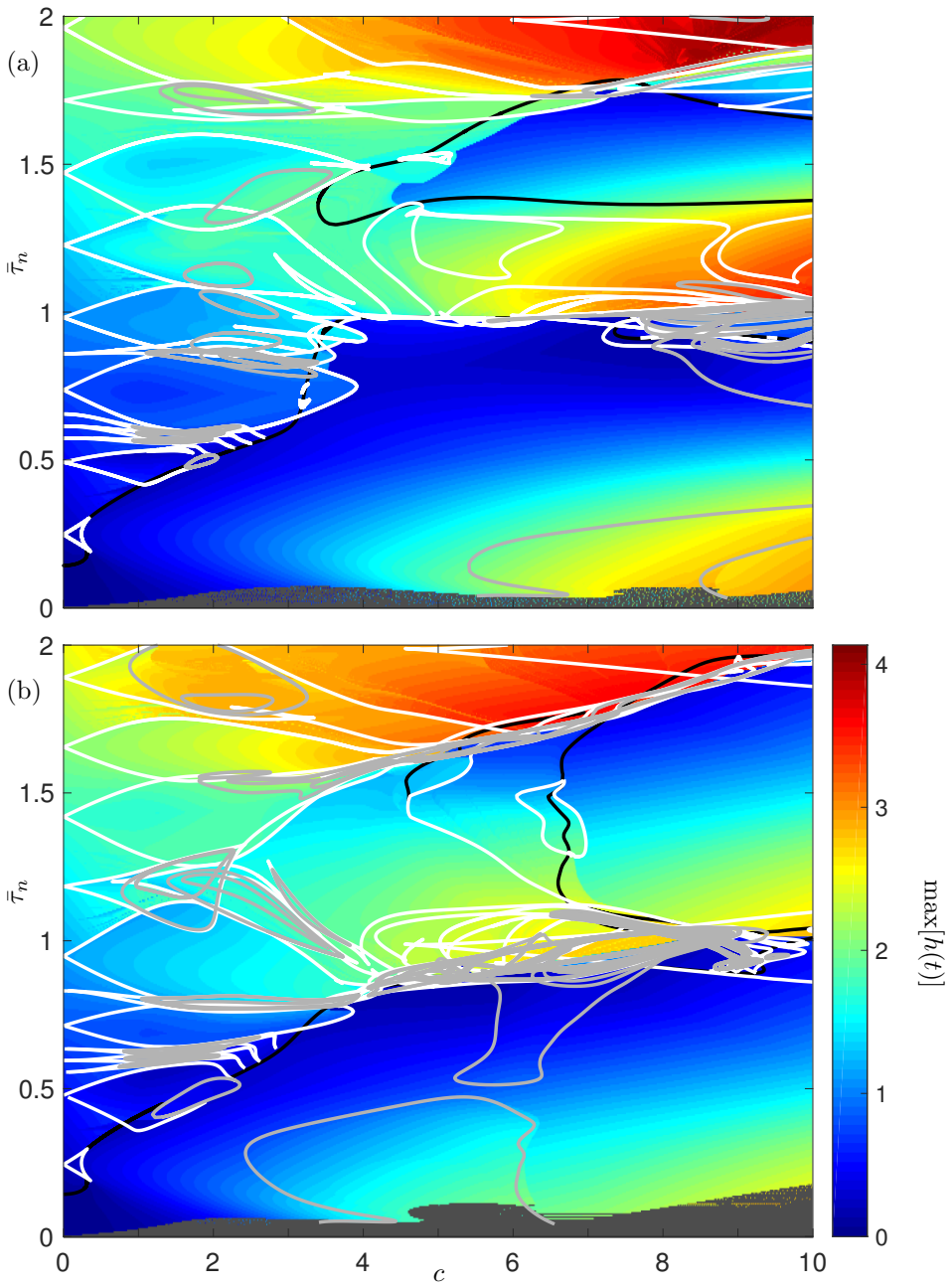

Figure 7. Bifurcation set and maximum map in the $(c, \bar{\tau}_n)$-plane of Eq. (1.1) with (2.6) for $\eta_c = 0.11$ and $\eta_e = 0.08$ (a) and $\eta_c = 0.22$ and $\eta_e = 0.04$ (b). Shown are black curves of torus bifurcations, white curves of saddle-node bifurcations of periodic orbits and grey curves of period-doubling bifurcations.

(c) Combined effects of the two types of state dependence

We now study the combined effects of both types of state dependence, that is, we consider $\eta_e > 0$ and $\eta_c > 0$. Figure 7 demonstrates that state dependence due to upwelling has a large effect on the overall bifurcation set when the ocean adjustment state dependence is also present. This is

surprising since state dependence due to upwelling on its own does not change the bifurcation set.

Panel (a) of Figure 7 considers the effect of the maximal nominal value $\eta_e = 0.08$ of upwelling on the case of a smaller ocean adjustment of $\eta_c = 0.11$ shown in Figure 4(a). The comparison shows that Figure 7(a) features a dramatic change in the way the different types of solutions are distributed across the $(c, \bar{\tau}_n)$-plane. In particular, the torus bifurcation curve appears to have split into two segments around $\bar{\tau}_n = 1.2$. In fact, as we checked but do not show here, even for $c > 40$ the two curves remain disconnected. This change of the bifurcation set is the result of a transition similar to the interacting torus bifurcation curves in Figure 5. Notice in Figure 7(a) how some resonance tongues have become significantly wider and overlap to a greater extent, resulting in larger regions of chaotic behaviour. We observe again the emergence of the period-doubling cluster near $\bar{\tau}_n = 1$, as well as the cusp bifurcations of the forcing dominated solutions near $(c, \bar{\tau}_n) = (6, 1)$ and near $(c, \bar{\tau}_n) = (6, 2)$.

Panel (b) of Figure 7 considers the effect of the nominal value $\eta_e = 0.04$ of upwelling on the case of a maximal ocean adjustment of $\eta_c = 0.22$ shown in Figure 4(b). The changes are not quite so pronounced, because the bifurcation diagram for $\eta_c = 0.22$ and $\eta_e = 0$ is already quite complex with torus bifurcation curves extending to large c. However, notice that in Figure 7(b) the period-doubling cluster near $\bar{\tau}_n = 1$ is now found for smaller values of c.

Finally, Figure 8 shows the bifurcation set for the maximal nominal ocean adjustment of $\eta_c = 0.22$ and the maximal nominal upwelling of $\eta_e = 0.08$. Here panel (a) shows the bifurcation set with the maximum map and panel (b) shows it with a map of where the maximal Lyapunov exponents of the respective solution is positive, that is, where the dynamics is chaotic. Comparing Figure 8 with Figure 3 clearly drives home the point that state dependence has a large effect on the bifurcation set of model (1.1) and, hence, on the observable dynamics. When comparing Figure 8(a) with Figure 7(b), we observe that increasing the upwelling to $\eta_e = 0.08$ result in the two large period-doubling bifurcations of the $0{:}1$ solutions to undergo a saddle transition near $\tau_n = 0.5$ and connect differently. Moreover, the period-doubling cluster now appears for even lower values of c. As Figure 8(b) shows, chaotic dynamics is associated with this period-doubling cluster. Indeed, comparison with Figure 3(b) clearly demonstrates that state dependence results in considerably more and larger regions where chaotic dynamics can be found. Interestingly, there is also a large region of chaotic dynamics for very low values of $\bar{\tau}_n$, near the boundary where the delay becomes negative.

(d) Interpretation for the ENSO system

By introducing a physically motivated non-constant delay time, we have made the DAO model more detailed. This model modification has led to dynamics that is expected to represent realistic aspects of the ENSO system. In the constant delay case, irregular (chaotic) behaviour could only be found for small pockets of the $(c, \bar{\tau}_n)$-plane and, as such, could not be considered a prominent feature of the model behaviour. In the state-dependent delay case, on the other hand, this type of behaviour is more prominent. Of particular interest here is the period-doubling cluster, which is the relatively large region with chaotic dynamics near $\bar{\tau}_n = 1$. Note that our discussion of suggested nominal values of the parameters $\bar{\tau}_e$, $\bar{\tau}_c$ and τ_w in Section 2 places the period-doubling cluster within the range of physically relevant values of $\bar{\tau}_n = \bar{\tau}_e + \bar{\tau}_c + \tau_w$. Since the emergence of chaotic behaviour in ENSO models has often been attributed to specific routes to chaos (i.e. the period-doubling [21,22,74], quasi-periodic [17,24,75] and intermittent [76] routes), we mention here that all these routes may be observed within the period-doubling cluster, depending on the chosen path through parameter space.

To show that the associated dynamics is indeed relevant for ENSO, Figure 9 displays time series and power spectra for an observational data set and an example attractor from model (1.1). Panel (a1) shows a time series for the Nino3 index, which is the averaged SST over 5°N–5°S and 150°W–90°W. It is calculated from the observational data set NOAA Optimum Interpolation SST V2 (Jan. 1982 – Dec. 2017) based on the analysis of in situ and satellite data [77]. Typically,

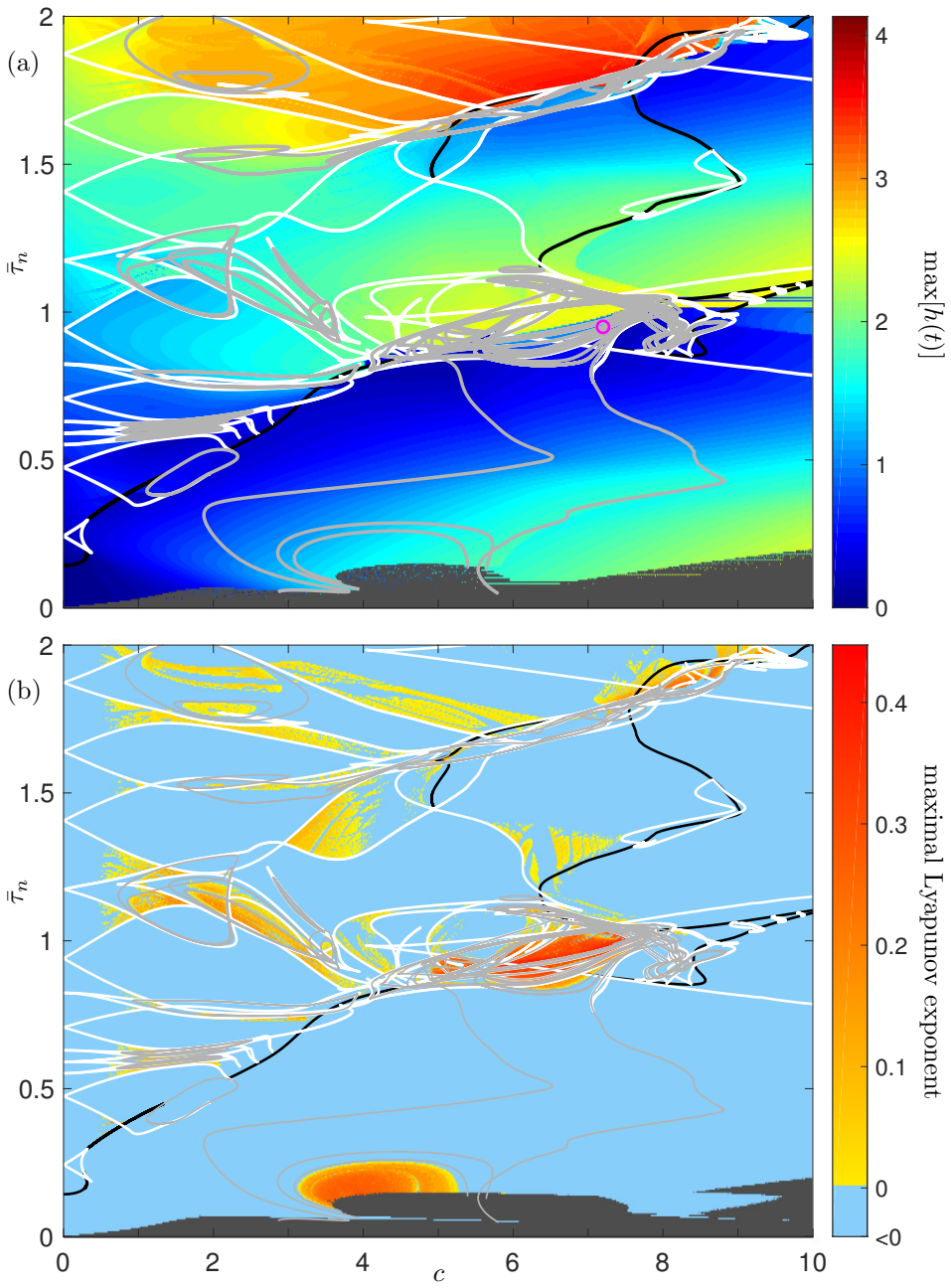

Figure 8. Bifurcation set and maximum map (a) and positive maximal Lyapunov exponent of solutions (b) in the $(c, \bar{\tau}_n)$-plane of Eq. (1.1) with (2.6) for $\eta_c = 0.22$ and $\eta_e = 0.08$. The magenta circle in panel (a) indicates the parameter choice for the time series in Figure 9.

for Nino3 the data is detrended by using a 5-month running mean. Here, we simply detrend linearly in order to preserve the seasonal cycle. The power spectrum in panel (a2) is calculated by using the Welch method with windows of length 15 years and overlapping across 12 years. The time series in panel (a1) demonstrates characteristic features of the ENSO system, including the irregularity of very distinct large peaks, representing El Niño events, both in terms of amplitude and occurrence. There is clearly a high degree of variability and, as we checked, the large peaks

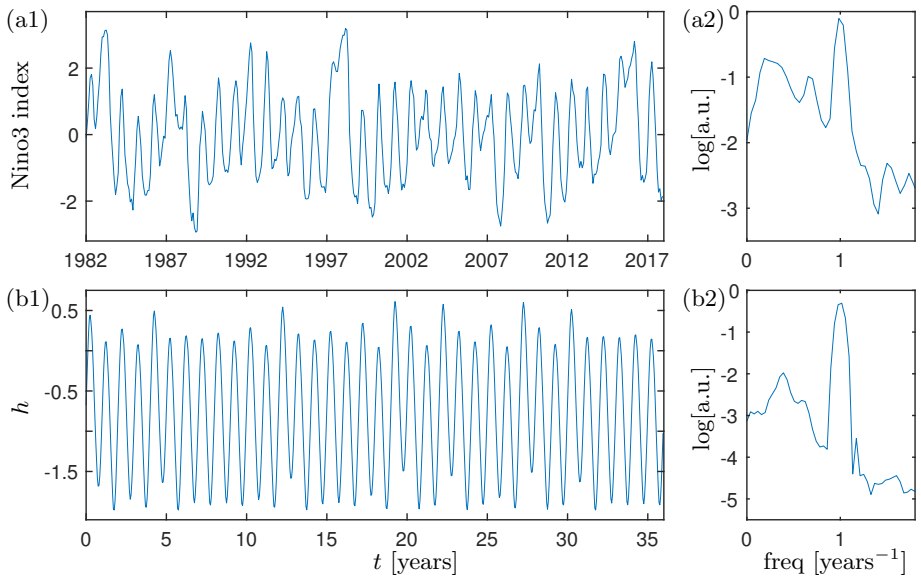

Figure 9. Panel (a1) shows a time series of the Nino3 index calculated from the observational data set NOAA Optimum Interpolation SST V2 (Jan. 1982 – Dec. 2017); the data is detrended linearly. Panel (a2) shows the corresponding power spectrum in arbitrary units [a.u.] calculated with the Welch method. Panels (b1) and (b2) show the same for an example attractor of Eq. (1.1) with (2.6) for $\eta_c = 0.22$ and $\eta_e = 0.08$ at the parameter point $(c, \bar{\tau}_n) = (7.2, 0.95)$, as indicated in Figure 8, and starting from the constant initial history $h \equiv 1$. Data for row (a) is provided by the Physical Sciences Division, Earth System Research Laboratory, NOAA, Boulder, Colorado.

tend to be seasonally locked. The influence of the seasons is evident in the power spectrum in panel (a2) with a distinct peak centred at 1 year. There are also two distinct peaks centred near 0.66 and 3.5 years, representing the time scales of ENSO variability. Note that the peak centred near 3.5 years is particularly broad.

The time series of the thermocline deviation h of model (1.1) in panel (b1) lies on a chaotic attractor that resides in the period-doubling cluster at $(c, \bar{\tau}_n) = (7.2, 0.95)$. It features irregularity in the form of relatively large peaks that occur every 4–8 years, as well as seasonal locking with a corresponding dominant frequency in panel (b2) centred at 1 year. The power spectrum also displays a broad peak centred near 2.5 years. Comparison between rows (a) and (b) of Figure 9 demonstrates that these two characteristic features of El Niño events from observational data (and many other models [18,24,56,78,79]) are captured by model (1.1). We find that the seasonal locking is very robust with respect to the choice of parameters. The number and distribution of El Niño peaks, on the other hand, depends on the choice of the parameters point in regions of overlapping p:q resonance tongues. Furthermore, the relative strengths between the peaks in the power spectrum, representing both seasonal and El Niño time scales can be influenced by the choice of the seasonal forcing strength c. We remark with regard to the amplitude of the oscillations in panel (b1), that one could calibrate the remaining model parameters b and κ in order to scale the variable h. Importantly, by using Figure 8 as a guide, solutions demonstrating fundamental ENSO characteristics can be found readily in the appropriate regions of parameter space. Therefore, we conclude that state-dependent delay associated with upwelling and ocean adjustment must be considered as a contributing mechanism for the observed irregular but seasonally-locked behaviour of the ENSO phenomenon.

In spite of the good agreement of the power spectra in Figure 9, row (b) does not feature the same degree of variability found in the observational data in row (a). Of course, the example solution represented in row (b) is calculated for the thermocline depth anomaly with

the conceptual model (1.1) with only a negative delayed feedback and forcing term. Exactly how the variable h translates to an observable such as Nino3 is not obvious, especially since Nino3 is a spatially averaged quantity and model (1.1) has no spatial component. Making a closer comparison between the dynamics of model (1.1) and climate observables is left for future work.

4. Summary and Discussion

The processes controlling the irregularity of the temporal variability of ENSO are still not satisfactorily determined and this hampers skilful prediction [8,9]. Certainly atmospheric noise, in particular westerly wind bursts, contribute to the irregularity of the ENSO variability and some literature is in support of the theory that ENSO is a stable, linear system subject to stochastic forcing [80–83]. However, there are also quite a few deterministic mechanisms that can give rise to chaotic behaviour, such as bursting phenomena [84,85], period-doubling [21,22,74] and nonlinear resonances with the seasonal cycle [17,24,75]. This motivates the study of conceptual ENSO models, which have been very useful in the past for investigating the interactions of known mechanisms and for discovering new physical mechanisms of variability.

The work presented here makes a contribution in this spirit by considering a quite simple conceptual ENSO model in the form of a DDE. Models of this type are known to efficiently represent physical processes, such as wave propagation and feedbacks [15]. Moreover, DDE models lend themselves to an investigation with advanced tools. As our study demonstrates, this is also the case when the delays that arise are no longer considered to be constant, which is an assumption in much of the previous literature in climate science and other fields. In particular, it is possible to ascertain whether and how state dependence of delays contributes to the overall dynamics of the feedback-driven system.

More specifically, we performed a study of the influence of additional and state-dependent delays arising from the interaction between the thermocline and the ocean surface. To this end, we incorporated state dependence of delays into a well-studied ENSO DDE model with only negative feedback and periodic forcing [19,35,70]. We derived state dependent delay terms for upwelling in the eastern Pacific and for ocean adjustment in the central Pacific, and then investigated their effect individually and also in combination. To capture important features of the overall dynamics, we considered the respective bifurcation sets in the $(c, \bar{\tau}_n)$-plane of the forcing strength c and the constant portion $\bar{\tau}_n$ of the overall delay. We demonstrated how an increasing complexity of the bifurcation set arises with increasing state dependence. Relevant levels of state dependence of the delays were shown to severely enhance resonance phenomena, leading to considerably larger regions with overlapping resonance tongues and associated peridod doublings and chaotic dynamics. The latter generate times series with characteristic features of the ENSO phenomenon, specifically, its irregular occurrence every few years in combination with seasonal locking. We remark that chaotic behaviour arising from nonlinear resonances has always been considered to be a less important mechanism of ENSO variability because the observed windows of its existence in parameter space were relatively small [25]. The widening of chaotic regions in the parameter space, as found here due to state-dependent delays, is hence highly relevant for attributing irregular ENSO variability more to deterministic processes rather than noise.

It is worth noting that other mechanisms may play a role in the complexity of the model dynamics. For example, the authors of [21] showed that the inclusion of additional Rossby wave modes and an asymmetric coupling function each increase the complexity of the dynamics of their ENSO delay-difference model. Furthermore, including positive delayed feedback due to Kelvin waves and asymmetry of the coupling each increase the complexity of the bifurcation diagram of the GZT DDE model studied here [20]. It is an interesting observation that in the state-dependent DDE model the breaking of symmetry, discussed in section 3(b), is achieved without the need of introducing an asymmetric coupling function, as was the case in [18,20,21].

The bifurcation sets presented here highlight the role of invariant tori in producing dynamical mechanisms resulting in complicated behaviour. The schematic bifurcation diagram in [86], based on simulation runs of a hybrid coupled general circulation model, also indicates the role of

torus dynamics in ENSO. The origins of dynamics on a torus in an intermediate coupled ocean-atmosphere model for the ENSO system was identified more thoroughly with continuation methods in [87]. A bifurcation set for the DDE ENSO model introduced in [18] is presented in Figure 6 of [88]. Like the bifurcation sets presented here, the authors of [88] found resonance tongues emanating from a curve of torus bifurcations; however, these resonance tongues appear not to interact with each other (at least over the parameter ranges considered). The bifurcation sets for a conceptual ENSO model presented in [84,85] do not feature resonance tongues, but still demonstrate the emergence of chaotic behaviour due to period-doubling. We remark that most of the dynamics we reported on involve 2-tori and their further bifurcations and could, hence, potentially be observed in models with dimension as low as 3. On the other hand, some more complicated dynamics might well be of higher dimension; a closer analysis of this is left for future work.

From a more general point of view, we demonstrated that state dependence of delays can have a serious impact on the dynamics, even when the constant-delay DDE already features complicated nonlinear behaviour. Our results follow on from the study by Calleja *et al.* [44], which showed that state dependence of delays alone can create surprisingly complicated nonlinear dynamics when the constant-delay DDE has only trivial, linear dynamics. Together, these results must be seen as a 'health warning' that delays should not simply be assumed to be constant as a matter of course. Given the simple form of the model we considered, with only delayed negative feedback and periodic forcing, we expect that our case study will be of interest to researchers from various other areas of application. The results presented here should provide motivation to investigate state-dependent delays more rigorously. A concrete example that is also discussed in this special issue concerns the dynamics driven by state-dependent delays in lasers with frequency-dependent feedback [50,51].

In the specific context of climate modelling, there are also several avenues for future work. The work presented here is an initial step in the analysis of the effects of state dependence on ENSO. For simplicity we have taken the state dependence of the delay to be linear. An interesting question from the modelling perspective is whether state-dependent delays can be derived explicitly from more complicated ENSO models of an intermediate complexity and, in particular, what mathematical form would they have. This paper might provide motivation for such a more quantitative analysis. One of the tools that can be used in this context is the Mori-Zwanzig formalism [89–91], which is a formal model reduction technique. Another focus for future work will be to study other physical mechanisms that may lead to state-dependent delays in the ENSO system. For example, a contributing factor to the delay times of the DAO paradigm is the position of the zone of ocean-atmosphere coupling in the central Pacific Ocean, which is closely associated with the western Pacific warm-pool. In fact, a state-dependent DDE for the position of the western Pacific warm-pool has already been suggested in [92], but has not yet been analysed. Finally, it will be of practical relevance to study the effect of atmospheric noise on the ENSO behaviour in DDE models with state-dependent delay.

Ethics. Not applicable.

Data Accessibility. Not applicable.

Authors' Contributions. AK carried out the numerical computations; all authors conceived of and designed the study, and drafted, read and approved the manuscript.

Competing Interests. The authors declare that they have no competing interests.

Funding. HAD acknowledges support by the Netherlands Earth System Science Centre (NESSC), financially supported by the Ministry of Education, Culture and Science (OCW), Grant no. 024.002.001.

Acknowledgements. We thank Jan Sieber for advice on implementing DDE-Biftool for the state-dependent delay case and Tony Humphries for advice on numerical integration of state-dependent DDEs. We are grateful to the Centre for eResearch at the University of Auckland for their help in facilitating this research through the use of the New Zealand eScience Infrastructure high-performance computing cluster.

Disclaimer. Not applicable.

References

1. Stocker T, Clarke G, Treut HL, Lindzen R, Meleshko V, Mugara R, Palmer T, Pierrehumbert R, Sellers P, Trenberth K, Willebrand J. 2001 Physical climate processes and feedbacks. In *Climate Change 2001: The Scientific Basis. Contribution of Working Group I to the Third Assessment Report of the Intergovernmental Panel on Climate Change* (ed. J Houghton, Y Ding, D Griggs, M Noguer, P van der Linden, X Dai, K Maskell, C Johnson), chapter 2, pp. 417–470. Cambridge, United Kingdom and New York, NY, USA: Cambridge University Press.
2. Bar-Eli K, Field RJ. 1998 Earth-average temperature: A time delay approach. *Journal of Geophysical Research: Atmospheres* **103**, 25949–25956.
3. Dijkstra HA. 2008 *Dynamical oceanography*. Springer Science & Business Media.
4. Dijkstra HA. 2005 *Nonlinear physical oceanography: a dynamical systems approach to the large scale ocean circulation and El Niño*, volume 28. Springer Science & Business Media.
5. Kaper H, Engler H. 2013 *Mathematics and climate*. SIAM.
6. Runge J, Petoukhov V, Kurths J. 2014 Quantifying the strength and delay of climatic interactions: The ambiguities of cross correlation and a novel measure based on graphical models. *Journal of Climate* **27**, 720–739.
7. Simonnet E, Dijkstra HA, Ghil M. 2009 Bifurcation analysis of ocean, atmosphere, and climate models. In *Handbook of Numerical Analysis*, volume 14, pp. 187–229. Elsevier.
8. Barnston AG, Tippett MK, L'Heureux ML, Li S, DeWitt DG. 2012 Skill of real-time seasonal ENSO model predictions during 2002–11: Is our capability increasing? *Bulletin of the American Meteorological Society* **93**, 631–651.
9. L'Heureux ML, Takahashi K, Watkins AB, Barnston AG, Becker EJ, Di Liberto TE, Gamble F, Gottschalck J, Halpert MS, Huang B, *et al.* 2017 Observing and predicting the 2015/16 El Niño. *Bulletin of the American Meteorological Society* **98**, 1363–1382.
10. Budyko MI. 1969 The effect of solar radiation variations on the climate of the earth. *tellus* **21**, 611–619.
11. Lorenz EN. 1963 Deterministic nonperiodic flow. *Journal of the atmospheric sciences* **20**, 130–141.
12. Neelin JD, Battisti DS, Hirst AC, Jin FF, Wakata Y, Yamagata T, Zebiak SE. 1998 ENSO theory. *Journal of Geophysical Research: Oceans* **103**, 14261–14290.
13. North GR. 1975 Theory of energy-balance climate models. *Journal of the Atmospheric Sciences* **32**, 2033–2043.
14. Stommel H. 1961 Thermohaline convection with two stable regimes of flow. *Tellus* **13**, 224–230.
15. Suarez MJ, Schopf PS. 1988 A delayed action oscillator for ENSO. *Journal of the atmospheric Sciences* **45**, 3283–3287.
16. Battisti DS, Hirst AC. 1989 Interannual variability in a tropical atmosphere-ocean model: Influence of the basic state, ocean geometry and nonlinearity. *Journal of the Atmospheric Sciences* **46**, 1687–1712.
17. Tziperman E, Stone L, Cane MA, Jarosh H. 1994 El Niño chaos: Overlapping of resonances between the seasonal cycle and the Pacific ocean-atmosphere oscillator. *Science* **264**, 72–74.
18. Tziperman E, Cane MA, Zebiak SE, Xue Y, Blumenthal B. 1998 Locking of El Niño's peak time to the end of the calendar year in the delayed oscillator picture of ENSO. *Journal of climate* **11**, 2191–2199.
19. Ghil M, Zaliapin I, Thompson S. 2008 A delay differential model of ENSO variability: parametric instability and the distribution of extremes. *Nonlinear Processes in Geophysics* **15**, 417–433.
20. Keane A, Krauskopf B, Postlethwaite C. 2016 Investigating irregular behavior in a model for the El Niño Southern Oscillation with positive and negative delayed feedback. *SIAM Journal on Applied Dynamical Systems* **15**, 1656–1689.
21. Münnich M, Cane MA, Zebiak SE. 1991 A study of self-excited oscillations of the tropical ocean-atmosphere system. Part II: Nonlinear cases.

Journal of the atmospheric sciences **48**, 1238–1248.
22. Cane MA, Münnich M, Zebiak SF. 1990 A study of self-excited oscillations of the tropical ocean-atmosphere system. Part I: Linear analysis.
Journal of the atmospheric sciences **47**, 1562–1577.
23. Zaliapin I, Ghil M. 2010 A delay differential model of ENSO variability — Part 2: Phase locking, multiple solutions and dynamics of extrema.
Nonlinear Processes in Geophysics **17**, 123–135.
24. Tziperman E, Cane MA, Zebiak SE. 1995 Irregularity and locking to the seasonal cycle in an ENSO prediction model as explained by the quasi-periodicity route to chaos.
Journal of the atmospheric sciences **52**, 293–306.
25. Jin FF, Neelin JD, Ghil M. 1996 El Niño/Southern Oscillation and the annual cycle: Subharmonic frequency-locking and aperiodicity.
Physica D-Nonlinear Phenomena **98**, 442–465.
26. Chang P, Ji L, Li H, Flügel M. 1996 Chaotic dynamics versus stochastic processes in El Nino–Southern Oscillation in coupled ocean-atmosphere models.
Physica D: Nonlinear Phenomena **98**, 301–320.
27. Słowiński P, Krauskopf B, Wieczorek S. 2015 Mode structure of a semiconductor laser with feedback from two external filters.
Discrete & Continuous Dynamical Systems-B **20**, 519–586.
28. Campbell SA. 2007 Time delays in neural systems.
In *Handbook of brain connectivity*, pp. 65–90. Springer.
29. Orosz G, Stépán G. 2006 Subcritical hopf bifurcations in a car-following model with reaction-time delay.
In *Proceedings of the Royal Society of London A: Mathematical, Physical and Engineering Sciences*, volume 462, pp. 2643–2670. The Royal Society.
30. Adimy M, Crauste F, Hbid ML, Qesmi R. 2010 Stability and Hopf bifurcation for a cell population model with state-dependent delay.
SIAM Journal on Applied Mathematics **70**, 1611–1633.
31. Blyuss KB, Kyrychko YN. 2010 Stability and bifurcations in an epidemic model with varying immunity period.
Bulletin of mathematical biology **72**, 490–505.
32. Driver RD. 2012 *Ordinary and delay differential equations*, volume 20.
Springer Science & Business Media.
33. Hale JK, Lunel SMV. 2013 *Introduction to functional differential equations*, volume 99.
Springer Science & Business Media.
34. Roose D, Szalai R. 2007 Continuation and bifurcation analysis of delay differential equations.
In *Numerical continuation methods for dynamical systems*, pp. 359–399. Springer.
35. Keane A, Krauskopf B, Postlethwaite C. 2015 Delayed feedback versus seasonal forcing: Resonance phenomena in an El Niño Southern Oscillation model.
SIAM Journal on Applied Dynamical Systems **14**, 1229–1257.
36. Engelborghs K, Luzyanina T, Samaey G. 2000 DDE-BIFTOOL: a Matlab package for bifurcation analysis of delay differential equations.
TW Report **305**.
37. Sieber J, Engelborghs K, Luzyanina T, Samaey G, Roose D. 2014 DDE-BIFTOOL Manual — Bifurcation analysis of delay differential equations.
arXiv preprint arXiv:1406.7144 .
38. Keane A, Krauskopf B, Postlethwaite CM. 2017 Climate models with delay differential equations.
Chaos: An Interdisciplinary Journal of Nonlinear Science **27**, 114309.
39. Insperger T, Stépán G. 2000 Stability of the milling process.
Periodica polytechnica mechanical engineering **44**, 47–57.
40. Kane DM, Shore KA. 2005 *Unlocking dynamical diversity: optical feedback effects on semiconductor lasers*.
John Wiley & Sons.
41. Humphries A, Bernucci D, Calleja R, Homayounfar N, Snarski M. 2016 Periodic solutions of a singularly perturbed delay differential equation with two state-dependent delays.
Journal of Dynamics and Differential Equations **28**, 1215–1263.
42. Sieber J. 2012 Finding periodic orbits in state-dependent delay differential equations as roots of algebraic equations.

Discrete & Continuous Dynamical Systems-A **32**, 2607–2651.
43. Sieber J. 2017 Local bifurcations in differential equations with state-dependent delay.
Chaos: An Interdisciplinary Journal of Nonlinear Science **27**, 114326.
44. Calleja RC, Humphries A, Krauskopf B. 2017 Resonance phenomena in a scalar delay differential equation with two state-dependent delays.
SIAM Journal on Applied Dynamical Systems **16**, 1474–1513.
45. Insperger T. 2011 Stick balancing with reflex delay in case of parametric forcing.
Communications in Nonlinear Science and Numerical Simulation **16**, 2160–2168.
46. Semenov V, Zakharova A, Maistrenko Y, Schöll E. 2016 Delayed-feedback chimera states: Forced multiclusters and stochastic resonance.
EPL (Europhysics Letters) **115**, 10005.
47. Sorrentino T, Quintero-Quiroz C, Aragoneses A, Torrent M, Masoller C. 2015 Effects of periodic forcing on the temporally correlated spikes of a semiconductor laser with feedback.
Optics express **23**, 5571–5581.
48. Insperger T, Stépán G, Turi J. 2007 State-dependent delay in regenerative turning processes.
Nonlinear Dynamics **47**, 275–283.
49. Craig M, Humphries AR, Mackey MC. 2016 A mathematical model of granulopoiesis incorporating the negative feedback dynamics and kinetics of G-CSF/neutrophil binding and internalization.
Bulletin of mathematical biology **78**, 2304–2357.
50. Martínez-Llinàs J, Porte X, Soriano MC, Colet P, Fischer I. 2015 Dynamical properties induced by state-dependent delays in photonic systems.
Nature communications **6**, 7425.
51. Fischer I PLACE-HOLDER: State-dependent delays in laser systems (to appear in this theme issue).
?? .
52. Neelin JD. 1991 The slow sea surface temperature mode and the fast-wave limit: Analytic theory for tropical interannual oscillations and experiments in a hybrid coupled model.
Journal of the atmospheric sciences **48**, 584–606.
53. Jin FF, Neelin JD. 1993 Modes of interannual tropical ocean-atmosphere interaction — A unified view. Part I: Numerical results.
Journal of the atmospheric sciences **50**, 3477–3503.
54. Neelin JD, Jin FF. 1993 Modes of interannual tropical ocean-atmosphere interaction — A unified view. Part II: Analytical results in the weak-coupling limit.
Journal of the atmospheric sciences **50**, 3504–3522.
55. Jin FF, Neelin D. 1993 Modes of interannual tropical ocean-atmosphere interaction — A unified view. Part III: Analytical results in fully coupled cases.
Journal of the atmospheric sciences **50**, 3523–3540.
56. Zebiak SE, Cane MA. 1987 A model El Niño–Southern Oscillation.
Monthly Weather Review **115**, 2262–2278.
57. Jin FF. 1997 An equatorial ocean recharge paradigm for ENSO. Part I: Conceptual model.
Journal of the Atmospheric Sciences **54**, 811–829.
58. Jin FF. 1997 An equatorial ocean recharge paradigm for ENSO. Part II: A stripped-down coupled model.
Journal of the Atmospheric Sciences **54**, 830–847.
59. Zelle H, Appeldoorn G, Burgers G, van Oldenborgh GJ. 2004 The relationship between sea surface temperature and thermocline depth in the eastern equatorial Pacific.
Journal of physical oceanography **34**, 643–655.
60. Harrison D, Vecchi GA. 2001 El niño and la niña?equatorial pacific thermocline depth and sea surface temperature anomalies, 1986–98.
Geophysical Research Letters **28**, 1051–1054.
61. Boulanger JP, Menkes C. 1995 Propagation and reflection of long equatorial waves in the Pacific Ocean during the 1992–1993 El Niño.
Journal of Geophysical Research: Oceans **100**, 25041–25059.
62. Chelton DB, Schlax MG. 1996 Global observations of oceanic Rossby waves.
Science **272**, 234–238.
63. Cao Y. 1996 Uniqueness of periodic solution for differential delay equations.
Journal of differential equations **128**, 46–57.

64. Chow SN, Walther HO. 1988 Characteristic multipliers and stability of symmetric periodic solutions of $\dot{x}(t) = g(x(t-1))$.
Transactions of the American Mathematical Society **307**, 127–142.
65. Nussbaum RD. 1979 Uniqueness and nonuniqueness for periodic solutions of $x'(t) = -g(x(t-1))$.
Journal of Differential Equations **34**, 25–54.
66. Kuznetsov YA. 2013 *Elements of applied bifurcation theory*, volume 112.
Springer Science & Business Media.
67. Broer H, Simó C, Tatjer JC. 1998 Towards global models near homoclinic tangencies of dissipative diffeomorphisms.
Nonlinearity **11**, 667.
68. Farmer JD. 1982 Chaotic attractors of an infinite-dimensional dynamical system.
Physica D: Nonlinear Phenomena **4**, 366–393.
69. Pomeau Y, Manneville P. 1980 Intermittent transition to turbulence in dissipative dynamical systems.
Communications in Mathematical Physics **74**, 189–197.
70. Keane A, Krauskopf B. 2018 Chenciner bubbles and torus break-up in a periodically forced delay differential equation.
Nonlinearity **31**, R165.
71. Amann A, Mortell MP, O'Reilly EP, Quinlan M, Rachinskii D. 2009 Mechanism of synchronization in frequency dividers.
IEEE Trans. on Circuits and Systems **56**, 190–199.
72. Tiberkevich VS, Khymyn RS, Tang HX, Slavin AN. 2014 Sensitivity to external signals and synchronization properties of a non-isochronous auto-oscillator with delayed feedback.
Scientific reports **4**, 3873.
73. Golubitsky M, Stewart I, Schaeffer DG. 2012 *Singularities and groups in bifurcation theory*, volume 2.
Springer Science & Business Media.
74. Chang P, Ji L, Wang B, Li T. 1995 Interactions between the seasonal cycle and El Nino–Southern Oscillation in an intermediate coupled ocean-atmosphere model.
Journal of the atmospheric sciences **52**, 2353–2372.
75. Jin FF, Neelin J, Ghil M. 1994 El Niño on the devil's staircase: Annual subharmonic steps to chaos.
Science **264**, 70–72.
76. Wang C, Weisberg RH, Yang H. 1999 Effects of the wind speed–evaporation–SST feedback on the El Niño–Southern Oscillation.
Journal of the atmospheric sciences **56**, 1391–1403.
77. Reynolds RW, Rayner NA, Smith TM, Stokes DC, Wang W. 2002 An improved in situ and satellite SST analysis for climate.
Journal of climate **15**, 1609–1625.
78. Rasmusson EM, Carpenter TH. 1982 Variations in tropical sea surface temperature and surface wind fields associated with the Southern Oscillation/El Niño.
Monthly Weather Review **110**, 354–384.
79. Neelin JD, Jin FF, Syu HH. 2000 Variations in ENSO phase locking.
Journal of Climate **13**, 2570–2590.
80. Eckert C, Latif M. 1997 Predictability of a stochastically forced hybrid coupled model of El Niño.
Journal of Climate **10**, 1488–1504.
81. Roulston MS, Neelin JD. 2000 The response of an ENSO model to climate noise, weather noise and intraseasonal forcing.
Geophysical research letters **27**, 3723–3726.
82. Thompson C, Battisti D. 2000 A linear stochastic dynamical model of ENSO. Part I: Model development.
Journal of Climate **13**, 2818–2832.
83. Thompson C, Battisti D. 2001 A linear stochastic dynamical model of ENSO. Part II: Analysis.
Journal of Climate **14**, 445–466.
84. Timmermann A, Jin FF, Abshagen J. 2003 A nonlinear theory for El Niño bursting.
Journal of the atmospheric sciences **60**, 152–165.

85. Guckenheimer J, Timmermann A, Dijkstra H, Roberts A. 2017 (Un) predictability of strong El Niño events.
Dynamics and Statistics of the Climate System **2**, dzx004.
86. Neelin JD. 1990 A hybrid coupled general circulation model for El Niño studies.
Journal of the Atmospheric Sciences **47**, 674–693.
87. Dijkstra HA, Neelin JD. 1995 On the attractors of an intermediate coupled ocean-atmosphere model.
Dynamics of atmospheres and oceans **22**, 19–48.
88. Krauskopf B, Sieber J. 2014 Bifurcation analysis of delay-induced resonances of the El-Niño Southern Oscillation.
In *Proc. R. Soc. A*, volume 470, p. 20140348. The Royal Society.
89. Mori H. 1965 A continued-fraction representation of the time-correlation functions.
Progress of Theoretical Physics **34**, 399–416.
90. Zwanzig R. 1964 On the identity of three generalized master equations.
Physica **30**, 1109–1123.
91. Boers N, Chekroun MD, Liu H, Kondrashov D, Rousseau DD, Svensson A, Bigler M, Ghil M. 2017 Inverse stochastic–dynamic models for high-resolution Greenland ice core records.
Earth System Dynamics **8**, 1171–1190.
92. Clarke AJ, Wang J, Van Gorder S. 2000 A simple warm-pool displacement ENSO model.
Journal of physical oceanography **30**, 1679–1691.